Wavefield reconstruction for velocity-stress elastodynamic Full Waveform Inversion

Ole Edvard Aaker[⋆], Espen Birger Raknes[⋆†], Ørjan Pedersen[⋆] and Børge Arntsen[‡]

[⋆]*Aker BP ASA, Trondheim, Norway*

e-mail: ole.edvard.aaker@akerbp.com, espen.birger.raknes@akerbp.com, orjan.pedersen@akerbp.com

[†]*Norwegian University of Science and Technology, Department of Electronic Systems, Trondheim, Norway*

[‡]*Norwegian University of Science and Technology, Department of Geoscience and Petroleum, Trondheim, Norway*

e-mail: borge.arntsen@ntnu.no

SUMMARY

Gradient computations in full waveform inversion (FWI) require calculating zero-lag cross-correlations of two wavefields propagating in opposite temporal directions. Lossless media permit accurate and efficient reconstruction of the incident field from recordings along a closed boundary, such that both wavefields propagate backwards in time. Reconstruction avoids storing wavefield states of the incident field to secondary storage, which is not feasible for many realistic inversion problems. We give particular attention to velocity-stress modelling schemes and propose a novel modification of a conventional reconstruction method derived from the elastodynamic Kirchhoff-Helmholtz integral. In contrast to the original formulation (in a previous related work), the proposed approach is well-suited for velocity-stress schemes. Numerical examples demonstrate accurate wavefield reconstruction in heterogenous, elastic media. A practical example using three-dimensional elastic FWI demonstrates agreement with the reference solution.

Key words: Full waveform inversion, elastic, reconstruction

1 INTRODUCTION

Full waveform inversion (FWI) and reverse time migration (RTM) are modern seismic inversion and imaging methods used to predict the properties of the subsurface utilizing recorded data of seismic wavefields. A common imaging condition in RTM consists of zero-lag cross-correlation of a forward modelled (incident) field with the inverse-extrapolated recorded wavefield (Etgen et al. 2009). In an optimization-type framework, FWI based on both gradient methods and iterative solution of Newton's system require zero-lag cross-correlation(s) of modelled and adjoint field(s) (Plessix 2006; Métivier et al. 2017). Furthermore, certain type of Bayesian inversion schemes utilize gradient information, such as the Hamiltonian Markov-Chain Monte Carlo algorithm (Neal 2012; Sen & Biswas 2017).

The cross-correlations involved in FWI gradient computations and (cross-correlation based) RTM both require wavefields that are propagating in opposite time directions to be available at the same time instance. This is computationally challenging to achieve using time-domain forward modelling schemes. A straight-forward solution to this problem is to first perform the forward modelling of the incident field, while storing its state at each required time step, either in memory or on secondary storage (e.g. disk). The stored states of the incident field are then read during the (reverse-time) modelling of the adjoint field, such that the incident and adjoint fields can be crosscorrelated to compute the gradient. This is hereby referred to as the wavefield snapshot method. For large 3D problems there is typically not enough memory nor local secondary storage available to store all required time instances of the incident field. Furthermore, secondary storage is a low bandwidth and high latency storage medium, which may give concerns to program performance. Several solutions have been designed to address these concerns, some of which we will briefly review here. Optimal checkpointing (Griewank & Walther 2002; Symes 2007) is a procedure which significantly reduces the amount of memory and/or storage required, at the cost of extra forward simulations. In this setting, the incident wavefield is constructed from its nearest saved wavefield snapshot by modelling forward in time to the timestep of the adjoint field. The recomputation ratio, defined as quotient between the actual and minimal amount of timesteps propagated for the incident field, completely determines the number of wavefield snapshots required to be stored, and vice versa (Symes 2007). A recomputation ratio typically less than five is achieved for seismic imaging and inversion problems with up 10,000 timesteps, given a parameter choice that optimally balances the memory requirements and the recomputation ratio (Griewank & Walther 2002; Symes 2007; Yang et al. 2016).

The relatively high recomputation ratio of optimal checkpointing has motivated developments of alternative methods to efficiently compute the gradient in time-domain FWI. One such method is to compress the incident field's contributions to the gradient kernels, which can be done in both time and

space (Fichtner et al. 2009; Boehm et al. 2016). Wavefield compression methods avoid any extra wave equation solutions and the memory requirements are, by design, reduced compared to the method of wavefield snapshots. Significant reductions in the memory requirements are particularly observed when accepting lossy compression techniques (Boehm et al. 2016), i.e. compression techniques that do not allow an exact recovery of the original signal. Lossy compression techniques do, however, require parameter selection in terms of the compression parameters, in turn controlling the achieved compression ratio, in order to ensure sufficient closeness between the inexact gradient calculated with compression and the true gradient (Boehm et al. 2016).

Reconstruction methods in lossless media offer an intermediate solution between optimal checkpointing and lossy wavefield compression. By utilizing a final state and suitable source functions, the incident field is reconstructed and propagated backwards in time alongside the adjoint field, providing simultaneous timestep availability. In turn, this achieves lower storage demands than the wavefield snapshot method and a lower recomputation ratio than optimal checkpointing. Reconstruction methods avoid parameter tuning for achieving a sufficiently accurate gradient, which acts to balance a higher recomputation ratio than what has been observed with lossy wavefield compression methods (Boehm et al. 2016). In the remainder of this article, we consider the usage of reconstruction methods for efficient gradient computations in time-domain FWI due to their well-balanced characteristics with respect to memory usage, recomputation ratio and accuracy. Different methods for wavefield reconstruction exist, each with distinct demands with regards to computational effort and memory usage. In the context of FWI and RTM, we are interested in utilizing the most efficient method to perform accurate reconstruction. We therefore start with a brief review of the options.

Immersive Boundary Conditions (IBCs) have demonstrated numerical accuracy in forward and inverse wavefield extrapolation (Broggini et al. 2017). In the general case IBCs require precomputation of a large number of Green's functions, and are therefore computationally costly. IBCs are hence not considered for reconstruction of the incident field.

On the other hand, finite-difference (FD) injection does not require any extra forward simulations for wavefield reconstruction (Robertsson & Chapman 2000). Some of its disadvantages include being only applicable to finite-difference schemes and requiring large amounts of memory for higher-order stencils. As explicit FD schemes represent a class of computational algorithms characterized by low operational intensity (Williams et al. 2009), their performance are typically bounded by the memory bandwidth rather than the peak arithmetic performance of the hardware.

In contrast to FD injection methods, interpreting wavefield representation theorems derived from reciprocity theorems as a sum of point sources (Morse & Feshbach 1953) enables the derivation of re-

construction methods compatible with any numerical discretization scheme, without precomputation requirements and with memory requirements independent of the accuracy of the numerical discretization. These attractive computational properties motivate the search for an elastodynamic reconstruction method derived from this formalism.

Mittet (1994) presented an elastodynamic reconstruction method based upon the corresponding Kirchhoff-Helmholtz integral, requiring the storage of six fields at a boundary (of width one grid cell) enclosing the medium of interest. Similarly, Vasmel & Robertsson (2016) utilized a wavefield representation derived from the acoustic reciprocity theorem of convolution type as source functions in a staggered-grid FD scheme, and presented applications to wavefield separation and reconstruction of the incident field in RTM.

Raknes & Weibull (2016) utilized the method of Mittet (1994) for reconstruction of the incident field in elastodynamic FWI, but only in an approximate sense as they neglected one of the source terms required by the method. The time-domain forward modelling scheme considered here is based on solving the first order velocity-stress system, consisting of the equations of motion and the time-derivative of the generalized stress-strain relationship. The original formulation in Mittet (1994) utilized a second-order acceleration-stress system. Implementation of this reconstruction method in velocity-stress schemes would require the time-integrated stress tensor to be available, which the numerical scheme does not provide. We therefore propose modifications to the reconstruction method, which also appear to provide certain numerical benefits compared to the original formulation.

This paper is organized as follows: For completeness, we first introduce the governing equations and the desired forward modelling scheme. Starting from the reciprocity theorem of correlation type, we present at an intermediate step a reconstruction method consistent with the one used in Mittet (1994). The challenges of this representation within the context of the modelling scheme are presented. We suggest analytical modifications which resolve these challenges. Examples from wavefield reconstruction and its usage in FWI are considered. Discussion and concluding remarks are given at the end. The appendices constitute a link to the method of Vasmel & Robertsson (2016) and also provide relations that complete the findings of the main text.

2 FUNDAMENTAL EQUATIONS AND THE NUMERICAL SCHEME

We consider elastodynamic wavefields characterized by the particle velocity $v_i(\mathbf{x}, t)$ and the stress tensor $\tau_{ij}(\mathbf{x}, t)$, with $i, j = 1, 2, 3$. The spatial coordinate axis is specified as $\mathbf{x} = (x_1, x_2, x_3)$, where x_i is the Cartesian coordinate along the i'th axis. The temporal axis coordinate is denoted by the letter t. We adopt the Einstein convention implying summation over repeated indices, unless otherwise

specified, with the exception being the lowercase letter t.

The elastodynamic equations of motion and the time derivative of the generalized stress-strain relationship for an elastodynamic wavefield in a lossless, inhomogenous anisotropic medium read (Aki & Richards 2002)

$$\rho(\mathbf{x})\partial_t v_i(\mathbf{x}, t) - \partial_j \tau_{ij}(\mathbf{x}, t) = f_i(\mathbf{x}, t), \tag{1}$$

$$\partial_t \tau_{ij}(\mathbf{x}, t) - c_{ijkl}(\mathbf{x})\partial_l v_k(\mathbf{x}, t) = -c_{ijkl}(\mathbf{x})h_{kl}(\mathbf{x}, t). \tag{2}$$

The quantity $\rho(\mathbf{x})$ is the volumetric mass density of the medium and $c_{ijkl}(\mathbf{x})$ is its stiffness tensor. The source terms of body force density and deformation rate density are $f_i(\mathbf{x}, t)$ and $h_{kl}(\mathbf{x}, t)$, respectively. The stress and stiffness tensors satisfy the following symmetry properties: $\tau_{ij} = \tau_{ji}$, $c_{ijkl} = c_{jikl} = c_{klij}$ (Aki & Richards 2002). The source type of deformation rate density satisfies $h_{kl} = h_{lk}$.

The impulse responses, commonly termed Green's functions, of equations 1 and 2 are obtained by substituting impulsive point sources as source functions. Independent source function types and polarizations give rise to independent Green's functions, and we explain our notation by example. An impulsive point source of deformation rate located at position $\mathbf{x}'$ and polarized in terms of component mn reads

$$h_{kl}(\mathbf{x}, t) = \frac{1}{2}\{\delta_{kn}\delta_{lm} + \delta_{lm}\delta_{kn}\}\delta(\mathbf{x} - \mathbf{x}')\delta(t), \tag{3}$$

whereas an impulsive point source of body force located at position $\mathbf{x}''$ and polarized in direction p reads

$$f_i(\mathbf{x}, t) = \delta_{ip}\delta(\mathbf{x} - \mathbf{x}'')\delta(t). \tag{4}$$

The quantity $\delta(\cdot)$ is the Dirac delta distribution, whereas the subscripted variant $\delta_{\cdot,\cdot}$ is the Kronecker delta. Substitution of equation 3 into equations 1 and 2 gives the wavefield response denoted by $v_i(\mathbf{x}, t) = G_{i,nm}^{v,h}(\mathbf{x}, t; \mathbf{x}')$ and $\tau_{ij}(\mathbf{x}, t) = G_{ij,nm}^{\tau,h}(\mathbf{x}, t; \mathbf{x}')$. Similarly, the elastodynamic wavefield induced by the source in equation 4 is denoted by $v_i(\mathbf{x}, t) = G_{i,p}^{v,f}(\mathbf{x}, t; \mathbf{x}'')$ and $\tau_{ij}(\mathbf{x}, t) = G_{ij,p}^{\tau,f}(\mathbf{x}, t; \mathbf{x}'')$.

A convenient temporal discretization scheme for solving the system of equations 1 and 2 is to use the temporally staggered finite-difference operator pair

$$\partial_t v_i(\mathbf{x}, n\Delta t) \approx \frac{1}{\Delta t} \sum_{\ell=1}^{L_d} \alpha_\ell [v_i(\mathbf{x}, (n + \frac{1}{2} + \ell - 1)\Delta t) - v_i(\mathbf{x}, (n + \frac{1}{2} - \ell)\Delta t)], \tag{5}$$

$$\partial_t \tau_{ij}(\mathbf{x}, (n + \frac{1}{2})\Delta t) \approx \frac{1}{\Delta t} \sum_{\ell=1}^{L_d} \alpha_\ell [\tau_{ij}(\mathbf{x}, (n + \ell)\Delta t) - \tau_{ij}(\mathbf{x}, (n - \ell - 1)\Delta t)], \tag{6}$$

on a temporal grid of size Δt, FD operator half-length L_d and coefficients α_ℓ. The application of the temporal differentation operator pair in equations 5 and 6 is compatible with any spatial discretization. We refer to this as the forward modelling scheme.

3 WAVEFIELD RECONSTRUCTION

3.1 Kirchhoff-Helmholtz type wavefield representation

We consider the space-frequency domain for deriving the desired representations for wavefield reconstruction. For generality we derive the reconstruction procedures in terms of Green's functions. We utilize the following temporal Fourier convention, introduced via the inverse Fourier transform of a function $\hat{g}(\mathbf{x}, \omega)$ in the space-frequency domain

$$g(\mathbf{x}, t) := \frac{1}{2\pi} \int_{-\infty}^{\infty} e^{j\omega t} \hat{g}(\mathbf{x}, \omega) \, d\omega. \tag{7}$$

The quantities $j = \sqrt{-1}$ and ω are the imaginary unit and the angular frequency, respectively. Equation 7 leads to the identity $\partial_t^n g(\mathbf{x}, t) \Leftrightarrow (j\omega)^n \hat{g}(\mathbf{x}, \omega)$. For real-valued quantities in the time-domain, time reversal is equivalent to complex conjugation in the frequency domain. From hereon, the dependency on frequency is omitted in all function arguments. Frequency dependence is denoted by the hat symbol, i.e. $\hat{g}(\mathbf{x}) = \hat{g}(\mathbf{x}, \omega)$. The medium parameters in lossless media are real-valued and frequency independent in the space-frequency domain.

The elastodynamic reciprocity theorem of correlation type is a representation theorem involving the interaction of an advanced and a retarded wavefield state, denoted states A and B respectively. With the two states defined with equal medium parameters throughout an arbitrary domain Ω with boundary $\partial\Omega$, this type of Rayleigh reciprocity theorem reads (de Hoop 1966; Aki & Richards 2002; Wapenaar & Fokkema 2006)

$$\int_\Omega d^3\mathbf{x} \left(-\hat{\tau}_{ij,A}^* \hat{h}_{ij,B} + \hat{v}_{i,A}^* \hat{f}_{i,B} - \hat{\tau}_{ij,B} \hat{h}_{ij,A}^* + \hat{v}_{i,B} \hat{f}_{i,A}^* \right)$$
$$= \oint_{\partial\Omega} d^2\mathbf{x} \left(-\hat{\tau}_{ij,A}^* \hat{v}_{i,B} - \hat{\tau}_{ij,B} \hat{v}_{i,A}^* \right) n_j. \tag{8}$$

When considering the time-reversed state (A) as a reverse-time extrapolator, equation 8 enables time-

reversed propagation of the wavefield in state B from recordings of it along the the closed boundary $\partial\Omega$ with normal vector $\mathbf{n} = (n_1, n_2, n_3)$. The correlation type reciprocity theorem can therefore be used to reconstruct the incident field in elastodynamic FWI gradient computations and cross-correlation based RTM imaging. We consider the Green's function in terms of stress due to an impulsive source of deformation rate as the inverse extrapolator (state A). For notational simplicity we consider the physical source to be of the same type as the reconstruction-type source, and therefore consider the following source functions

$$\hat{h}_{ij,A}(\mathbf{x}) = \delta(\mathbf{x} - \mathbf{x}_A)\frac{1}{2}\{\delta_{ip}\delta_{jq} + \delta_{iq}\delta_{jp}\}, \tag{9}$$

$$\hat{h}_{ij,B}(\mathbf{x}) = \delta(\mathbf{x} - \mathbf{x}_B)\frac{1}{2}\{\delta_{in}\delta_{jm} + \delta_{im}\delta_{jn}\}. \tag{10}$$

The sources of body force density are chosen to be equal to zero for both states. Inserting the source quantities and their corresponding wavefield responses into equation 8 and utilizing source-receiver reciprocity of stress due to a deformation rate source gives

$$\hat{G}^{\tau,h}_{pq,nm}(\mathbf{x}_A; \mathbf{x}_B) + \chi(\mathbf{x}_B)\{\hat{G}^{\tau,h}_{pq,nm}(\mathbf{x}_A; \mathbf{x}_B)\}^* =$$
$$\oint_{\partial\Omega} d^2\mathbf{x} \left(\{\hat{G}^{\tau,h}_{ij,pq}(\mathbf{x}; \mathbf{x}_A)\}^* \hat{G}^{v,h}_{i,nm}(\mathbf{x}; \mathbf{x}_B) + \hat{G}^{\tau,h}_{ij,nm}(\mathbf{x}; \mathbf{x}_B)\{\hat{G}^{v,h}_{i,pq}(\mathbf{x}; \mathbf{x}_A)\}^*\right)n_j, \tag{11}$$

where $\chi(\mathbf{x})$ is the characteristic function

$$\chi(\mathbf{x}) := \begin{cases} 0 & x \notin \Omega, \\ 1 & x \in \Omega. \end{cases} \tag{12}$$

The left hand side of equation 11 retrieves the causal Green's function, at position $\mathbf{x}_A$, provided that the location of the source, $\mathbf{x}_B$, is outside the domain Ω. Vice versa, the corresponding homogenous Green's function is retrieved. For notational simplicity we ignore the term involving the characteristic function, and discuss the implications later.

Rewriting the particle-velocity term $\{\hat{G}^{v,h}_{i,pq}(\mathbf{x}; \mathbf{x}_A)\}^*$ using the equations of motion in a region void of sources of body force type gives

$$\hat{G}^{\tau,h}_{pq,nm}(\mathbf{x}_A; \mathbf{x}_B) = \oint_{\partial\Omega} d^2\mathbf{x} \left(\{\hat{G}^{\tau,h}_{ij,pq}(\mathbf{x}; \mathbf{x}_A)\}^* \hat{G}^{v,h}_{i,nm}(\mathbf{x}; \mathbf{x}_B)\right.$$
$$\left. - \hat{G}^{\tau,h}_{ij,nm}(\mathbf{x}; \mathbf{x}_B)\frac{1}{j\omega\rho(\mathbf{x})}\{\partial_l G^{\tau,h}_{il,pq}(\mathbf{x}; \mathbf{x}_A)\}^*\right)n_j. \tag{13}$$

Equation 13 is an elastodynamic Kirchhoff-Helmholtz integral. Utilizing the properties of the delta distribution, the definition of its distributional derivative and source-receiver reciprocity gives

$$\hat{G}^{\tau,h}_{pq,nm}(\mathbf{x};\mathbf{x}_s) = \int_\Omega d^3\mathbf{x}' \left\{\hat{G}^{\tau,h}_{pq,ij}(\mathbf{x};\mathbf{x}')\right\}^* \oint_{\partial\Omega} d^2\mathbf{x}_r \left(\partial'_j \delta(\mathbf{x}' - \mathbf{x}_r)\frac{\hat{G}^{\tau,h}_{ik,nm}(\mathbf{x}_r;\mathbf{x}_s)}{j\omega\rho(\mathbf{x}_r)}n_k \right.$$
$$\left. + \delta(\mathbf{x}' - \mathbf{x}_r)\hat{G}^{v,h}_{i,nm}(\mathbf{x}_r;\mathbf{x}_s)n_j\right). \tag{14}$$

Indices and coordinates have been renamed for the sake of clarity. Equation 14 is consistent with the representation used by Mittet (1994), only stated in the context of the first-order equations of motion and stress-strain relationship. Although it is not the final representation, it is time to give attention to how the wavefield reconstruction should be interpreted and implemented.

3.2 The anti-causal Huygen's principle

The stress field $\hat{\tau}_{pq}$ due to a source of deformation rate density $\hat{h}_{kl}$ can be shown to satisfy the hyperbolic wave-equation

$$\hat{\mathcal{L}}_{klpq}(\mathbf{x})\hat{\tau}_{pq}(\mathbf{x}) = j\omega\hat{h}_{kl}(\mathbf{x}), \tag{15}$$

with the linear wave-equation operator $\hat{\mathcal{L}}_{klpq}$ given by

$$\hat{\mathcal{L}}_{klpq}(\mathbf{x})[\cdot] = \omega^2 s_{klpq}(\mathbf{x})[\cdot] + \frac{1}{2}\partial_l\left(\frac{1}{\rho(\mathbf{x})}\partial_h\delta_{pk}\delta_{qh}\,[\cdot]\,\right) + \frac{1}{2}\partial_k\left(\frac{1}{\rho(\mathbf{x})}\partial_h\delta_{pl}\delta_{qh}\,[\cdot]\,\right), \tag{16}$$

and where the compliance tensor s_{klpq} satisfies the relationship $s_{klpq}c_{pqnm} = \frac{1}{2}(\delta_{kn}\delta_{lm} + \delta_{km}\delta_{ln})$. The notation $[\cdot]$ denotes where the operator is applied. The Green's function $\hat{G}^{\tau,h}_{pq,nm}(\mathbf{x};\mathbf{x}')$ satisfies equation 15 with a corresponding impulsive source function of deformation rate $\hat{h}_{kl}(\mathbf{x}) = \delta(\mathbf{x} - \mathbf{x}')\frac{1}{2}\{\delta_{km}\delta_{ln} + \delta_{kn}\delta_{lm}\}$. The correlation type reciprocity theorem (equation 8) permits an anti-causal Huygen's principle when considering rigid- or free-surface boundary conditions and suitable source functions

$$\hat{\tau}_{pq}(\mathbf{x}) = \int_\Omega d^3\mathbf{x}' \left\{\hat{G}^{\tau,h}_{pq,ij}(\mathbf{x};\mathbf{x}')\right\}^* \{-\hat{h}_{ij}(\mathbf{x}')\}. \tag{17}$$

By comparison, one can identify that the reconstruction stated in equation 14 is of the form of the anti-causal Huygen's principle, with the source function being

$$\hat{h}_{ij,nm}(\mathbf{x};\mathbf{x}_s) = -\oint_{\partial\Omega} d^2\mathbf{x}_r \left(\partial_j\delta(\mathbf{x} - \mathbf{x}_r)\frac{\hat{G}^{\tau,h}_{ik,nm}(\mathbf{x}_r;\mathbf{x}_s)}{j\omega\rho(\mathbf{x}_r)}n_k + \delta(\mathbf{x} - \mathbf{x}_r)\hat{G}^{v,h}_{i,nm}(\mathbf{x}_r;\mathbf{x}_s)n_j\right). \tag{18}$$

Although the anti-causal Huygen's principle is derived under specific boundary conditions, this imposes no limitation on the validity of the reconstruction method. In the situation of wavefield recon-

struction we have rewritten the power flux through $\partial\Omega$, represented as the boundary interaction in the correlation type reciprocity theorem, as a source function (Morse & Feshbach 1953).

3.3 Modifications of the source function

The frequency-domain velocity-stress system with the given source function for wavefield reconstruction reads

$$j\omega\rho(\mathbf{x})\hat{G}^{v,h}_{i,nm}(\mathbf{x};\mathbf{x}_s) - \partial_j\hat{G}^{\tau,h}_{ij,nm}(\mathbf{x};\mathbf{x}_s) = 0, \tag{19}$$

and

$$j\omega\hat{G}^{\tau,h}_{ij,nm}(\mathbf{x};\mathbf{x}_s) - c_{ijkl}(\mathbf{x})\partial_l\hat{G}^{v,h}_{k,nm}(\mathbf{x};\mathbf{x}_s) = -c_{ijkl}(\mathbf{x})\oint_{\partial\Omega}d^2\mathbf{x}_r\Big(-\partial_l\delta(\mathbf{x}-\mathbf{x}_r)\frac{\hat{G}^{\tau,h}_{ke,nm}(\mathbf{x}_r;\mathbf{x}_s)}{j\omega\rho(\mathbf{x}_r)}n_e$$
$$-\delta(\mathbf{x}-\mathbf{x}_r)\hat{G}^{v,h}_{k,nm}(\mathbf{x}_r;\mathbf{x}_s)n_l\Big). \tag{20}$$

Evidently, usage of the source function in equation 18 for wavefield reconstruction requires the time-integrated stress tensor, $\frac{1}{j\omega}\hat{G}^{\tau,h}_{ik,nm}(\mathbf{x}_r;\mathbf{x}_s)$, to be injected. When solving the time-domain velocity-stress system (equations 1-2) with the physical source, the field quantities provided are naturally the particle velocities and the stress tensor. Hence, not all field quantities for the reconstruction sources can be provided by the forward modelling scheme. This is in contrast to the second-order acceleration-stress method of Mittet (1994). Although one can approximately obtain the time-integrated stress tensor by temporal integration procedures, we suggest rather to make analytical modifications to the reconstruction type source function.

We therefore consider the (possibly) modified fields $\hat{\mathcal{V}}_{i,nm}(\mathbf{x};\mathbf{x}_s)$ and $\hat{\mathcal{T}}_{ij,nm}(\mathbf{x};\mathbf{x}_s)$, defined in the same inhomogenous anisotropic medium as $\hat{G}^{v,h}_{i,nm}(\mathbf{x};\mathbf{x}_s)$ and $\hat{G}^{\tau,h}_{ij,nm}(\mathbf{x};\mathbf{x}_s)$, satisfying

$$j\omega\rho\hat{\mathcal{V}}_{i,nm} - \partial_j\hat{\mathcal{T}}_{ij,nm} = \hat{\mathcal{F}}_{i,nm}, \tag{21}$$

$$j\omega\hat{\mathcal{T}}_{ij,nm} - c_{ijkl}\partial_l\hat{\mathcal{V}}_{k,nm} = -c_{ijkl}\hat{\mathcal{H}}_{kl,nm}. \tag{22}$$

The source functions of body force and deformation rate are respectively given by

$$\hat{\mathcal{F}}_{i,nm}(\mathbf{x};\mathbf{x}_s) = \rho(\mathbf{x})\oint_{\partial\Omega}d^2\mathbf{x}_r\Big(\delta(\mathbf{x}-\mathbf{x}_r)\frac{\hat{G}^{\tau,h}_{ke,nm}(\mathbf{x}_r;\mathbf{x}_s)}{\rho(\mathbf{x}_r)}n_e\Big) \tag{23}$$

and

$$\hat{\mathcal{H}}_{kl,nm}(\mathbf{x};\mathbf{x}_s) = \oint_{\partial\Omega}d^2\mathbf{x}_r\Big(-\delta(\mathbf{x}-\mathbf{x}_r)\hat{G}^{v,h}_{k,nm}(\mathbf{x}_r;\mathbf{x}_s)n_l\Big). \tag{24}$$

Isolating $\hat{\mathcal{V}}_{k,nm}$ in the equations of motion and inserting the resulting expression into the stress-strain relationship gives

$$j\omega\hat{\mathcal{T}}_{ij,nm} - c_{ijkl}\partial_l \frac{1}{j\omega\rho}\partial_j\hat{\mathcal{T}}_{kj,nm} = c_{ijkl}\partial_l \frac{\hat{\mathcal{F}}_{k,nm}}{j\omega\rho} - c_{ijkl}\hat{\mathcal{H}}_{kl,nm}. \tag{25}$$

The quantity $\frac{1}{j\omega\rho(\mathbf{x})}\partial_j\hat{\mathcal{T}}_{kj,nm}(\mathbf{x};\mathbf{x}_s)$ is recognized as $\hat{G}^{v,h}_{k,nm}(\mathbf{x};\mathbf{x}_s)$ under the assumption that $\hat{\mathcal{T}}_{ij,nm}(\mathbf{x};\mathbf{x}_s) = \hat{G}^{\tau,h}_{ij,nm}(\mathbf{x};\mathbf{x}_s)$. Assume for now that this is true. Substituting equations 23 and 24 for the modified source functions into equation 25 then gives

$$j\omega\hat{\mathcal{T}}_{ij,nm}(\mathbf{x};\mathbf{x}_s) - c_{ijkl}(\mathbf{x})\partial_l\hat{G}^{v,h}_{k,nm}(\mathbf{x};\mathbf{x}_s) = -c_{ijkl}(\mathbf{x})\oint_{\partial\Omega} d^2\mathbf{x}_r\Big(-\partial_l\delta(\mathbf{x}-\mathbf{x}_r)\frac{\hat{G}^{\tau,h}_{ke,nm}(\mathbf{x}_r;\mathbf{x}_s)}{j\omega\rho(\mathbf{x}_r)}n_e$$
$$-\delta(\mathbf{x}-\mathbf{x}_r)\hat{G}^{v,h}_{k,nm}(\mathbf{x}_r;\mathbf{x}_s)n_l\Big). \tag{26}$$

By comparing equations 20 and 26 it is obvious that the assumed equivalence $\hat{\mathcal{T}}_{ij,nm} = \hat{G}^{\tau,h}_{ij,nm}$ holds. Hence, simultaneous usage of the source functions of body force and deformation rate in equations 23 and 24 yield the same wavefield reconstruction as the source function of deformation rate in equation 18. The advantages of the new source functions, compared to the one in equation 18, are:

(a) All field-quantities in the source functions are directly available from the forward modelling. There is no need to integrate the stress tensor in time.

(b) The modified source functions require no shifting of the stress tensor in time, c.f. equations 5 and 6.

(c) When implemented in spatially staggered-grid finite-difference schemes, it requires only *one* set of finite-difference coefficients, namely those of the original, staggered finite-difference stencil. In contrast, the approach of Mittet (1994) requires a second set of FD coefficients belonging to a non-staggered central difference stencil. Any potential spectral mismatch between staggered and non-staggered finite-difference operators is therefore avoided.

(d) It requires no implementation of the derivative of the Dirac delta distribution.

When implementing the source functions in equations 23 and 24 one has a degree of freedom whether to either implement the boundary integral explicitly, or to utilize the sifting properties of the Dirac delta distribution. The latter method consists of simply injecting (properly weighted) versions of the recorded field at the reconstruction boundary $\partial\Omega$ during reverse-time propagation. The two methods are equivalent when composite Riemann summation is used for the calculation of the boundary integral, and the discretized approximations of the Dirac delta distribution are properly normalized and satisfy a (discrete) sifting property. Both methods allow any source contributions not aligned with the points/degrees of freedom of the discretized computational domain to be accurately interpolated.

3.4 On the the location of the physical source

Beyond equation 11 we ignored the second term on the left-hand side, involving the time reversed variant of the Green's function. This quantity contributes if and only if the original source at position $\mathbf{x}_s$ was inside the reconstruction domain Ω. Using equation 15 for $\hat{G}^{\tau,h}_{pq,mn}(\mathbf{x};\mathbf{x}_s)$ and its time-reversal, and adding the two equations we get

$$\hat{\mathcal{L}}_{klpq}\hat{G}^{\tau,h}_{pq,mn}(\mathbf{x};\mathbf{x}_s) + \left\{ \hat{\mathcal{L}}_{klpq}\hat{G}^{\tau,h}_{pq,mn}(\mathbf{x};\mathbf{x}_s) \right\}^* = j\omega\delta(\mathbf{x}-\mathbf{x}_s)\frac{1}{2}\{\delta_{km}\delta_{ln} + \delta_{kn}\delta_{lm}\}$$
$$- j\omega\delta(\mathbf{x}-\mathbf{x}_s)\frac{1}{2}\{\delta_{km}\delta_{ln} + \delta_{kn}\delta_{lm}\}, \qquad (27)$$

$$\hat{\mathcal{L}}_{klpq}\left(\hat{G}^{\tau,h}_{pq,mn}(\mathbf{x};\mathbf{x}_s) + \{\hat{G}^{\tau,h}_{pq,mn}(\mathbf{x};\mathbf{x}_s)\}^* \right) = \hat{\mathcal{L}}_{klpq}\hat{\mathcal{G}}^{\tau,h}_{pq,mn}(\mathbf{x};\mathbf{x}_s) = 0. \qquad (28)$$

Evidently, the quantity $\hat{G}^{\tau,h}_{pq,mn}(\mathbf{x};\mathbf{x}_s) + \{\hat{G}^{\tau,h}_{pq,mn}(\mathbf{x};\mathbf{x}_s)\}^*$ is the homogenous Green's function $\hat{\mathcal{G}}^{\tau,h}_{pq,mn}(\mathbf{x};\mathbf{x}_s)$ (Oristaglio 1989; Wapenaar & Fokkema 2006). In order to reconstruct only the *causal* Green's function, with source position $\mathbf{x}_s \in \Omega$, one must subtract the original source function during the inverse extrapolation.

4 NUMERICAL EXAMPLES

For the numerical examples we use the staggered-grid finite-difference scheme of Virieux (1986), with higher-order derivative approximations, as the spatial discretization of the velocity-stress system. Similarly, shifting operators are used for shifting wavefield quantities between the reference and staggered grids. The latter are required for both recording stress and the particle velocities on the boundary, and for injection of the reconstruction sources. Approximations to the Dirac delta convolutional interpolation operator are employed as the shifting operators (Fornberg 1988; Mittet & Arntsen 2000). In the examples that follow, we implemented the reconstruction source functions with explicit calculation of the boundary integrals involved, similar to the procedure in Mittet (1994).

The spatial finite-difference approximation used for all numerical examples utilizes a stencil with half-length eight and group-velocity optimized coefficients (Holberg 1987). The level of accuracy for the interpolators need to be consistent with the spatial accuracy of the FD scheme (Mittet 1994; Vasmel & Robertsson 2016). Hence, the same half-length and optimization criterion were employed for generating the coefficients of the shifting operators.

4.1 Reconstruction in a homogenous region with an elastic free surface

We consider a homogenous region on a 20 m spatial grid, with an elastic free surface at the top and the remaining boundaries are absorbing. A diagonal source of deformation rate h_{ii}, exciting only P-

waves, with a 20 Hz central frequency Ricker wavelet was placed within the reconstruction domain Ω. Fig. 1 compares the modelled and reconstructed field along with their differences in terms of τ_{12}. In agreement with theory, the wavefield is only reconstructed within the reconstruction domain. Herein the reconstructed and modelled fields demonstrate good agreement.

4.2   Reconstruction inside the elastic Gullfaks model

We consider reconstruction of an elastic wavefield within a heterogenous region of an isotropic model of the Gullfaks field, offshore Norway. The model has spatially varying ρ, v_p and v_s parameters, where the characteristic contrasts are similar across the parameters. The v_p, v_s and ρ models are shown in Fig. 2, where the boundary $\partial\Omega$ of the reconstruction domain Ω is denoted by the dashed black lines. A diagonal source of deformation rate h_{ii} with a 20 Hz central frequency Ricker wavelet is placed in the middle of Ω. The top boundary is a free surface, whereas the remaining boundaries are set to be absorbing. Fig. 3 compares the modelled and reconstructed fields in terms of both τ_{11} and τ_{12}. As in the previous example, the field is reconstructed only within Ω and is herein in good agreement with the modelled field.

4.3   3D Elastodynamic FWI problem

We consider a 3D elastic inversion problem on a subset of the SEG/EAGE Overthrust model. The region considered contains shallow channels and various, curved interfaces. A water layer of thickness 200 m was added to create a marine model, thus resembling an offshore exploration setting. The shear-wave velocity model was generated using the Greenberg-Castagna relationship (Greenberg & Castagna 1992), whereas the volumetric mass density was kept constant at a value corresponding to water. The initial model was generated using Gaussian smoothing of the true model, except that the uppermost part of the seabed is kept equal to the true model in order to avoid inversion complexities arising from surface waves. In order to not introduce any false interfaces, a small smoothing zones is applied underneath. The true and initial models are compared in Figs. 4 and 5. They are both consistently discretized using a uniform grid spacing of 25 m. The proposed wavefield reconstruction method is utilized for efficient gradient computations involving the adjoint field and the reconstructed modelled field. For reference, the results are compared with the inversion result generated using the same parameters, where wavefield snapshots are used for the modelled field in the gradient computations.

The acquisition geometry design corresponds to a realistic OBN setup, with 13 receiver cables separated by a 400 m distance. Along each cable, the distance between the receivers is 25 m. A total

of 200 shots were considered, spread out along five sail lines with a 700 m distance across the lines. The source function was assumed to be known and corresponded to an 8 Hz central frequency Ricker wavelet. The least-squares misfit function was used to quantify the data misfit. The optimization procedure employed was the Polak–Ribière variant of Non-Linear Conjugate Gradients (Polak & Ribiere 1969), utilizing a parabolic linesearch method. The linesearches were still required to satisfy the Armijo condition (Nocedal & Wright 2006). The compressional and shear wave velocities were simultaneously inverted for. In order to reduce the computational demands of this example, we employed cyclic shot subsampling with four batches à 50 shots (Ha & Shin 2013). An outer loop was used to loop over the FWI subproblems solved on a per batch basis. We refer to the iterations of the outer loop as outer iterations. Due to the rather low number of shots per batch, Gaussian smoothing of the computed gradients was performed in order to minimize gradient artefacts caused by subsampling.

The wavefield snapshot and the reconstruction runs used similar or exactly equal amount of iterations throughout the batches and outer repetitions. The last shot batch used exactly eight iterations in total across the two methods, whereas the last repetition of the first batch allowed four extra iterations (compared to 12 iterations in the reconstruction run) to be performed in the wavefield snapshots method. The inverted compressional velocity distribution is compared across the two runs at a slice through the horizontal x_2 dimension in Fig. 6. The shallow parts of the model, particularly the channel system, appears to be well resolved. A vertical slice through the uppermost channel is shown in Fig. 7, and comparing with Fig. 5a) confirms that the FWI models provide a good reproduction of this feature. Certain cycle-skipping artefacts are however visible as non-physical stripes or reflectors, especially in the deeper parts. They can be attributed to the usage of high frequencies and lack of a multi-scale approach to the inversion. The scope of this example is but to demonstrate the equivalence between the wavefield snapshot and reconstruction methods in FWI, and the artefacts should therefore not be too concerning. Deeper parts of the model are not well resolved, owing partly to the choice of optimization procedure, lack of gradient weighting, short recording times and a restricted offset range. The shear wave velocity distributions are compared in Figs. 8 and 9. The inverted v_s models demonstrate characteristics very similar to the inverted v_p models.

It is clear that the inverted models across the two runs are in agreement with one another. The gradient of the objective function with respect to the shear wave velocity at the first iteration of the first shot batch is compared across the two runs in Fig. 10. For completeness, the misfit evolution of the first

shot batch of the two inversion runs are compared. This is graphically depicted for the iterations in common in Fig. 11. The misfit evolutions demonstrate similar behavior across the two runs.

5   DISCUSSION

5.1   On the reconstruction method

This paper has presented modifications of the reconstruction method of Mittet (1994) in order to remove its need of the time-integrated stress tensor when implemented in velocity-stress schemes. The alternative would be to provide this quantity by the usage of temporal integration procedures on the stress tensor recorded at the boundaries. Empirically, we observed that such an approach resulted in substantial numerical leakage, even when using spectral procedures. The modifications here presented were developed in order to remove this limitation. Another potential source of errors stems from the handling of the corner points of Cartesian aligned boundary surfaces, as it appears that the normal vector of the boundary is discontinuous there. Utilizing a simple weighting factor $\frac{1}{2}$ for the corner points themselves greatly reduced any artefacts related to the discontinuity of the boundary. Difficulties within the corner-point region were also observed by Vasmel & Robertsson (2016) for higher-order finite-difference schemes, and it appears that this is the greatest source of errors present. The usage of boundary surfaces aligned with the Cartesian axes was chosen primarily for computational efficiency, as the shifting of wavefield quantities onto the boundary is very simple compared to using an arbitrarily shaped boundary. Although our numerical examples utilize the finite-difference method for spatial discretization, the proposed reconstruction method can be applied in virtually any numerical scheme that solve the same equations for forward modelling. In Appendix A we demonstrate that the proposed source functions are analytically equivalent to the elastodynamic generalization of the Multiple Point Sources (MPS) approach of Vasmel & Robertsson (2016).

The main text discussed reconstruction of an elastodynamic wavefield using the Green's function in terms of stress due to an (impulsive) source of deformation rate. Appendix B demonstrates the same concept with the inverse extrapolator being the Green's function in terms of particle velocity due to an impulsive source of body force. The latter approach gives analytically equivalent source contributions for wavefield reconstruction. In the main text we also considered the physical source to be of the same type as the reconstruction-type source, i.e. of deformation rate type. In Appendix C we briefly demonstrate that physical sources of body force are equally valid.

Although the reconstruction method is accurate, when applied to iterative optimization methods (such as FWI) one should not expect the misfit evolutions, nor the inverted models, to be exactly equal. Even ill-posed *linear* problems are highly sensitive to data perturbations (Hansen 1998), at times even floating point errors, see e.g. Björck et al. (1998). Nonetheless, good agreement was observed between the reconstruction and snapshot inversion runs in the FWI example presented. The extra repetitions allowed in the first shot batch in the snapshot run performed only inconsequentally small steps, by backtracking, and reduced the then present misfit only by less than 0.05%, corresponding to a total reduction in misfit of 0.00375%.

5.2   Fluid-solid contacts

Some of the most popular numerical modelling schemes do not treat fluid-solid contacts optimally, which may in turn affect the quality of the achieved reconstruction, depending on the geometrical set-up of the reconstruction domain. There are two main ways of handling the liquid-solid interface: the *partitioned* and the *monolithic* approach (Hou et al. 2012). The monolithic approach uses only the elastodynamic equations and treat the boundary conditions implicitly by allowing the medium parameters to vary arbitrarily. The partitioned approach uses different partial differential equations in the acoustic and elastic subdomains and consider the explicit coupling between the two. Monolithic modelling schemes based on popular numerical methods such as finite-differences and classical finite/spectral element methods assume and/or enforce continuity of the particle velocity everywhere within the model (Komatitsch et al. 2000). However, because the tangential components of the stress tensor are zero at the interface, the tangential particle velocities are discontinuous across the fluid-solid interface. Within these specific monolithic schemes we identify two problems related to placing a reconstruction boundary close to a fluid-solid interface. The first is the well-known problem of excitation of parasitic modes when placing sources close to the interface. The second problem is unique to the staggered-grid FD method and relates to the fact that the numerical interpolators, used for shifting of staggered wavefield quantities, assume function continuity within the extent of the interpolation stencil. This is violated at fluid-solid interfaces. Both problems can be handled by placing the reconstruction boundary sufficiently away from the liquid-solid interface. It should be noted that the difficulties around liquid-solid interfaces is not directly related to the theory of the reconstruction scheme. If used with a numerical solver such as discontinuous Galerkin projection (Käser & Dumbser 2008), interfaces between fluids and solids should give no issues for arbitrarily placed reconstruction boundaries.

5.3   Dissipative media

Reconstruction of the incident field for RTM and FWI by usage of the correlation type reciprocity theorem is not directly applicable in dissipative media. Reconstructing the exact forward wavefield, i.e. such that it would match its corresponding state during forward propagation, would require it to gain energy upon inverse extrapolation. In such a situation, the expressions involving the correlation type reciprocity theorem would include a volumetric integral term compensating for the energy dissipated during forward propagation. The time-reversed propagation would then often suffer from numerical instabilities. It seems natural to pursue alternative methods for efficient FWI and RTM.

The optimal checkpointing and wavefield compression methods are, on the other hand, general procedures applicable to any wavefield physics scenario. In view of the potential instabilities of reconstruction methods, either of these methods appear as sound choices for efficient FWI and RTM in dissipative media, although the recomputation ratio of optimal checkpointing might be practically challenging. Yang et al. (2016) proposed the hybrid method termed *checkpointing-assisted reverse-forward simulation* (CARFS) which combines reconstruction and optimal checkpointing methods in order to reduce the recomputation ratio, while ensuring a numerically stable result. The algorithm chooses locally in time between forward propagation from wavefield snapshots or wavefield reconstruction, depending on the stability of inverse extrapolation with energy amplification. The stability is assessed by monitoring the total energy of the system (Yang et al. 2016). The reconstruction method presented in this paper is compatible with the CARFS algorithm. Another alternative is to perform frequency-domain gradient computations with time-domain modelling schemes. The procedure is then to calculate a discrete Fourier transform at appropriate timesteps in modelling of both the incident and adjoint fields (Sirgue et al. 2008).

6   CONCLUSION

The motivation of this paper was the possibility to perform efficient RTM and FWI gradient computations with time-domain, velocity-stress forward modelling schemes in lossless media. The Kirchhoff-Helmholtz integral method of Mittet (1994) is a computationally and memory-efficient reconstruction method. As shown however, it is not directly suited for implementation in the velocity-stress system. We mitigated this by considering analytical modifications of the source functions essential to the method. The modifications appear to provide some numerical benefits compared to the original formulation. Via an alternative path, but from a common starting point, we demonstrated that the suggested source functions are analytically exactly equal to the elastodynamic generalization of the MPS source functions in Vasmel & Robertsson (2016).

The wavefield reconstruction examples demonstrate accurate reconstruction of the forward modelled field. As shown, this holds equally well in both homogenous and heterogenous media.

We considered a realistic 3D elastic multiparameter inversion problem, where the reconstruction procedure was used for efficient gradient computations. The results were compared to a reference solution where wavefield snapshots were employed in the computation of the gradient. The results generated by either method are in good agreement with one another.

ACKNOWLEDGMENTS

REFERENCES

Aki, K. & Richards, P. G., 2002. *Quantitative seismology*, University Science Books.

Björck, Å., Elfving, T., & Strakos, Z., 1998. Stability of Conjugate Gradient and Lanczos Methods for Linear Least Squares Problems, *SIAM Journal on Matrix Analysis and Applications*, **19**(3), 720–736.

Boehm, C., Hanzich, M., de la Puente, J., & Fichtner, A., 2016. Wavefield compression for adjoint methods in full-waveform inversion, *Geophysics*.

Broggini, F., Vasmel, M., Robertsson, J. O. A., & van Manen, D.-J., 2017. Immersive boundary conditions: Theory, implementation, and examples, *Geophysics*, **82**(3), 1MJ–Z23.

de Hoop, A. T., 1966. An elastodynamic reciprocity theorem for linear, viscoelastic media, *Applied Scientific Research*, **16**(1), 39–45.

Etgen, J., Gray, S. H., & Zhang, Y., 2009. An overview of depth imaging in exploration geophysics, *Geophysics*, **74**(6), WCA5–WCA17.

Fichtner, A., Kennett, B. L., Igel, H., & Bunge, H. P., 2009. Full seismic waveform tomography for uppermantle structure in the Australasian region using adjoint methods, *Geophysical Journal International*.

Fornberg, B., 1988. Generation of Finite Difference Formulas on Arbitrarily Spaced Grids, *Mathematics of Computation*, **51**(184), 699.

Greenberg, M. L. & Castagna, J. P., 1992. Shear-wave Velocity Estimation In Porous Rocks: Theoretical Formulation, Preliminary Verification And Applications, *Geophysical Prospecting*, **40**(2), 195–209.

Griewank, A. & Walther, A., 2002. Algorithm 799: revolve: an implementation of checkpointing for the reverse or adjoint mode of computational differentiation, *ACM Transactions on Mathematical Software*.

Ha, W. & Shin, C., 2013. Efficient Laplace-domain full waveform inversion using a cyclic shot subsampling method, *Geophysics*, **78**(2), R37–R46.

Hansen, P. C., 1998. *Rank-Deficient and Discrete Ill-Posed Problems*, Society for Industrial and Applied Mathematics.

Holberg, O., 1987. Computational Aspects Of The Choice Of Operator And Sampling Interval For Numerical Differentiation In Large-scale Simulation Of Wave Phenomena, *Geophysical Prospecting*, **35**(6), 629–655.

Hou, G., Wang, J., & Layton, A., 2012. Numerical Methods for Fluid-Structure Interaction — A Review, *Communications in Computational Physics*.

Käser, M. & Dumbser, M., 2008. A highly accurate discontinuous Galerkin method for complex interfaces between solids and moving fluids, *Geophysics*, **73**(3), T23–T35.

Komatitsch, D., Barnes, C., & Tromp, J., 2000. Wave propagation near a fluid-solid interface: A spectral-element approach, *Geophysics*, **65**(2), 623–631.

Métivier, L., Brossier, R., Operto, S., & Virieux, J., 2017. Full Waveform Inversion and the Truncated Newton Method, *SIAM Review*.

Mittet, R., 1994. Implementation of the Kirchhoff integral for elastic waves in staggered-grid modeling schemes, *Geophysics*, **59**(12), 1894–1901.

Mittet, R. & Arntsen, B., 2000. General source and receiver positions in coarse-grid finite-difference schemes, *Journal of Seismic Exploration*.

Morse, P. & Feshbach, H., 1953. *Methods of Theoretical Physics*, McGraw-Hill Book Comp., Inc., New York, Toronto, London.

Neal, R. M., 2012. MCMC using Hamiltonian dynamics, *In Handbook of Markov Chain Monte Carlo*, pp. (pp. 113–162). CRC Press.

Nocedal, J. & Wright, S., 2006. *Numerical Optimization 2nd Ed*.

Oristaglio, M. L., 1989. An inverse scattering formula that uses all the data, *Inverse Problems*.

Plessix, R. E., 2006. A review of the adjoint-state method for computing the gradient of a functional with geophysical applications.

Polak, E. & Ribiere, G., 1969. Note sur la convergence de méthodes de directions conjuguées, *ESAIM: Mathematical Modelling and Numerical Analysis - Modélisation Mathématique et Analyse Numérique*, **3**(R1), 35–43.

Raknes, E. B. & Weibull, W., 2016. Efficient 3D elastic full-waveform inversion using wavefield reconstruction methods, *Geophysics*, **81**(2), R45–R55.

Robertsson, J. O. A. & Chapman, C. H., 2000. An efficient method for calculating finite-difference seismograms after model alterations, *Geophysics*, **65**(3), 907–918.

Sen, M. K. & Biswas, R., 2017. Transdimensional seismic inversion using the reversible jump Hamiltonian Monte Carlo algorithm, *Geophysics*, **82**(3), R119–R134.

Sirgue, L., T. Etgen, J., & Albertin, U., 2008. 3D Frequency Domain Waveform Inversion Using Time Domain Finite Difference Methods, in *70th EAGE Conference and Exhibition incorporating SPE EUROPEC 2008*.

Symes, W. W., 2007. Reverse time migration with optimal checkpointing, *GEOPHYSICS*.

Vasmel, M. & Robertsson, J. O. A., 2016. Exact wavefield reconstruction on finite-difference grids with

minimal memory requirements, *Geophysics*, **81**(6), T303–T309.

Virieux, J., 1986. P-SV wave propagation in heterogeneous media: Velocity-stress finite-difference method, *Geophysics*, **51**(4), 889–901.

Wapenaar, K. & Fokkema, J., 2006. Green's function representations for seismic interferometry, *Geophysics*, **71**(4), SI33–SI46.

Williams, S., Waterman, A., & Patterson, D., 2009. Roofline: An Insightful Visual Performance Model for Multicore Architecture, *Communications of the ACM*.

Yang, P., Brossier, R., Métivier, L., & Virieux, J., 2016. Wavefield reconstruction in attenuating media: A checkpointing-assisted reverse-forward simulation method, *Geophysics*, **81**(6), R349–R362.

Figs.
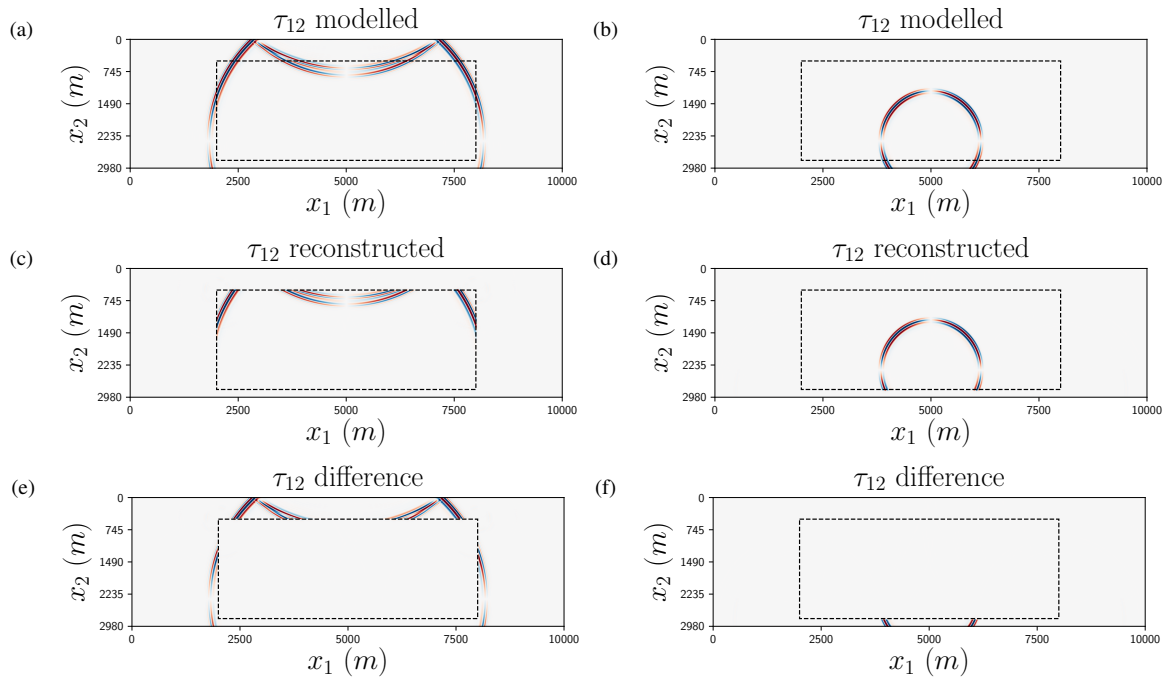
Fig. 1: Reconstruction within a homogenous region with an elastic free surface. Figs. a), c) and e) show the modelled, reconstructed and difference between the two in terms of τ_{12} at time $t = 1.4$ s. Figs. b), d) and f) show the modelled, reconstructed and difference between the two in terms of τ_{12} at time $t = 0.6$ s. The minimum and maximum values of the colorscale have been clipped in order to emphasize all events and any errors. The colorscales at each simulation time is the same for all wavefield components.
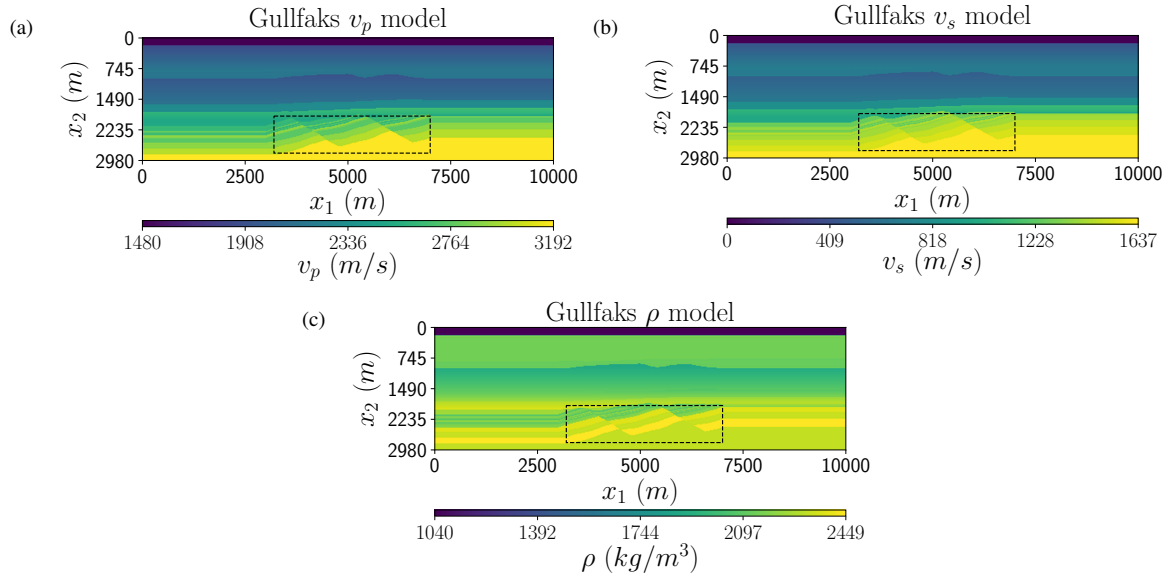
Fig. 2: a) The compressional wave velocity distribution of the Gullfaks model b) The shear wave velocity distribution of the Gullfaks model. c) The mass density distribution of the Gullfaks model. The boundary $\partial\Omega$ is denoted by the dashed black lines.
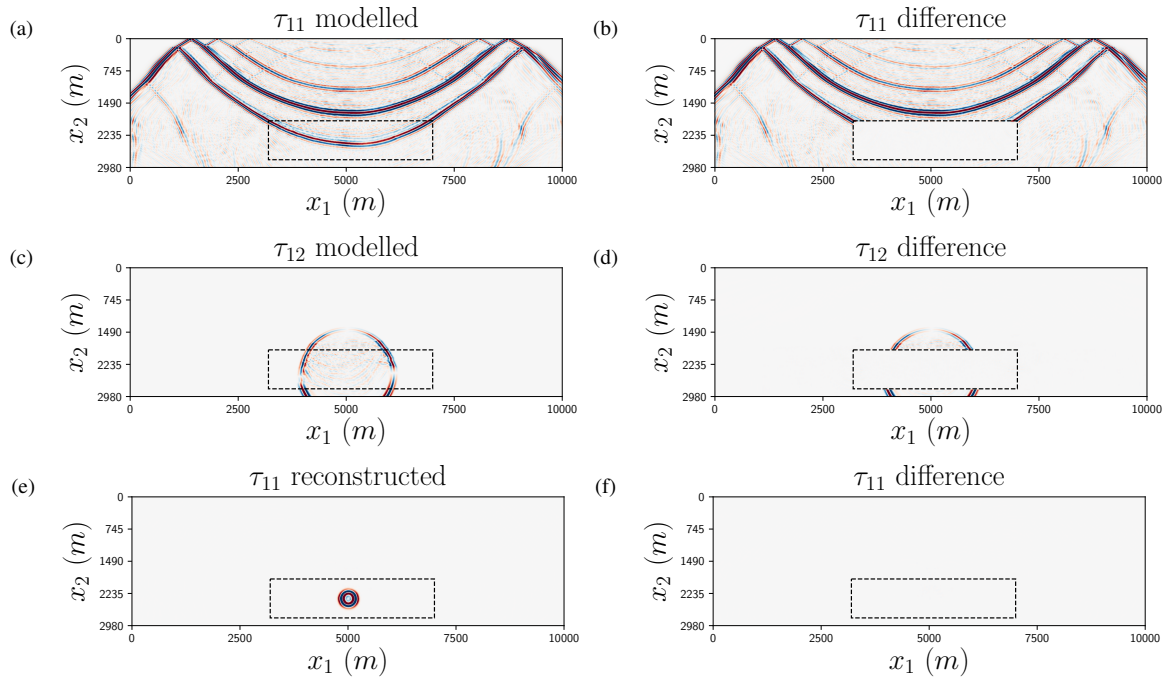

Fig. 3: Reconstruction within the Gullfaks model: a) and b) show the modelled τ_{11} and its difference to the reconstructed field at time $t = 2.1$ s. c) and d) show the modelled τ_{12} its difference to the reconstructed field at time $t = 0.5$ s. e) and f) show the reconstructed τ_{11} the difference between it and the modelled field at time $t = 0.2$ s.
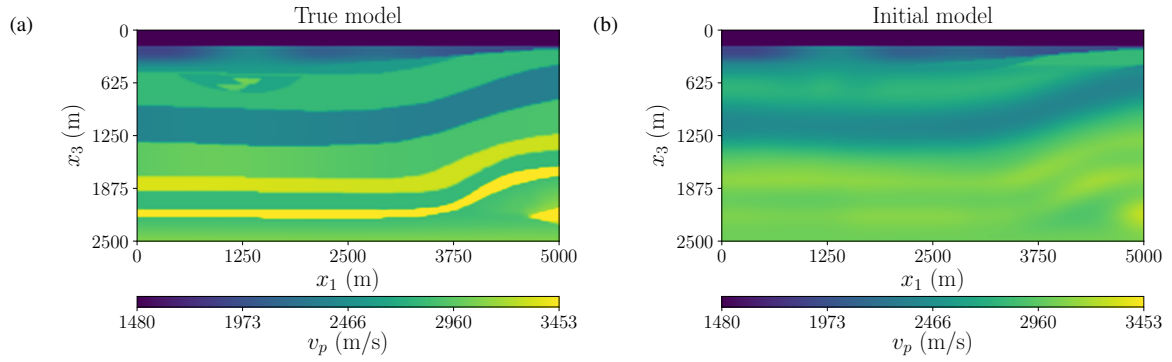
Fig. 4: The true a) and initial b) v_p distribution of the modified SEG/EAGE Overthrust model at $x_2 = 1250$ m.
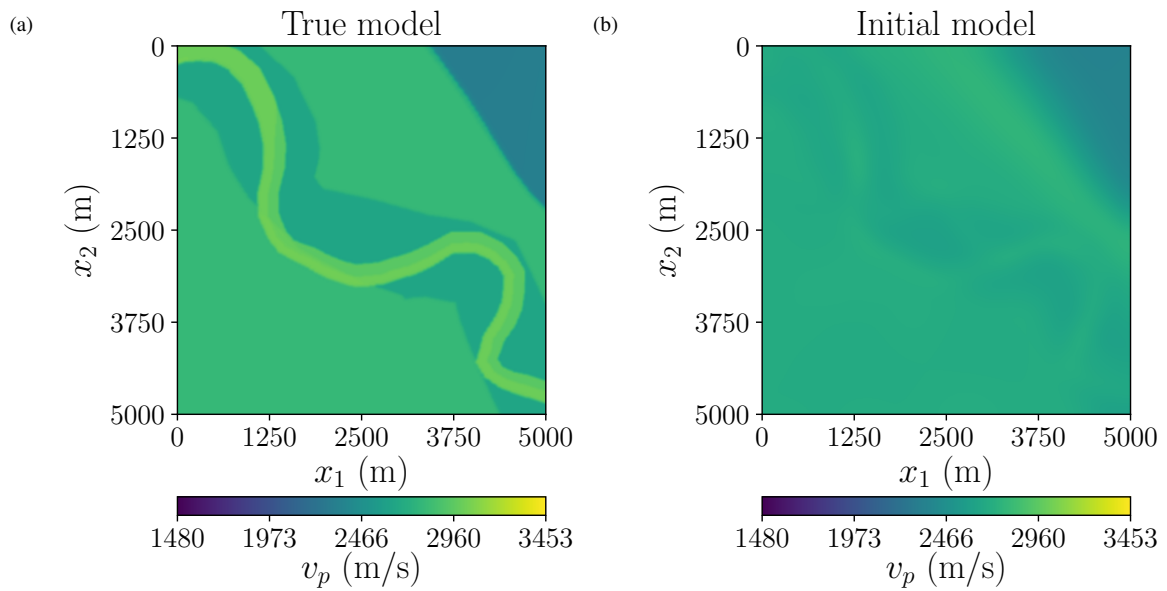
Fig. 5: The true a) and initial b) v_p distribution of the modified SEG/EAGE Overthrust model at $x_3 = 575$ m.
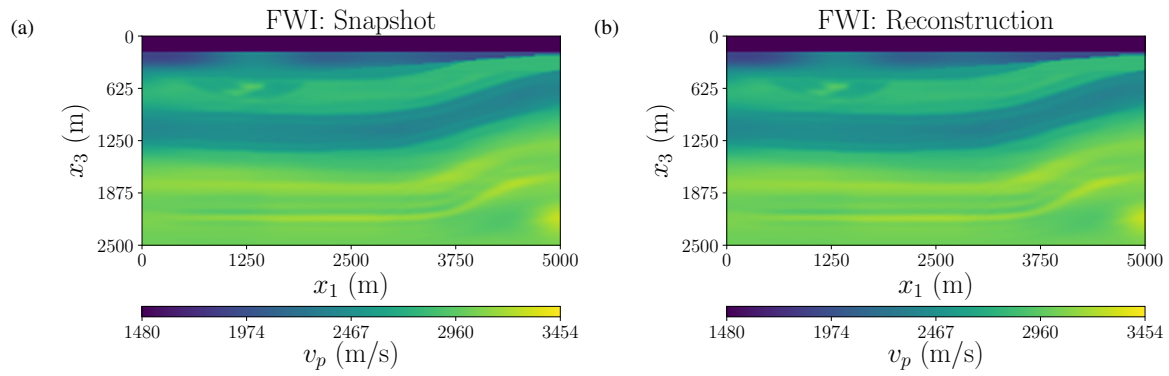
Fig. 6: The inverted v_p distributions at $x_2 = 1250$ m using a) wavefield snapshots and b) reconstruction.
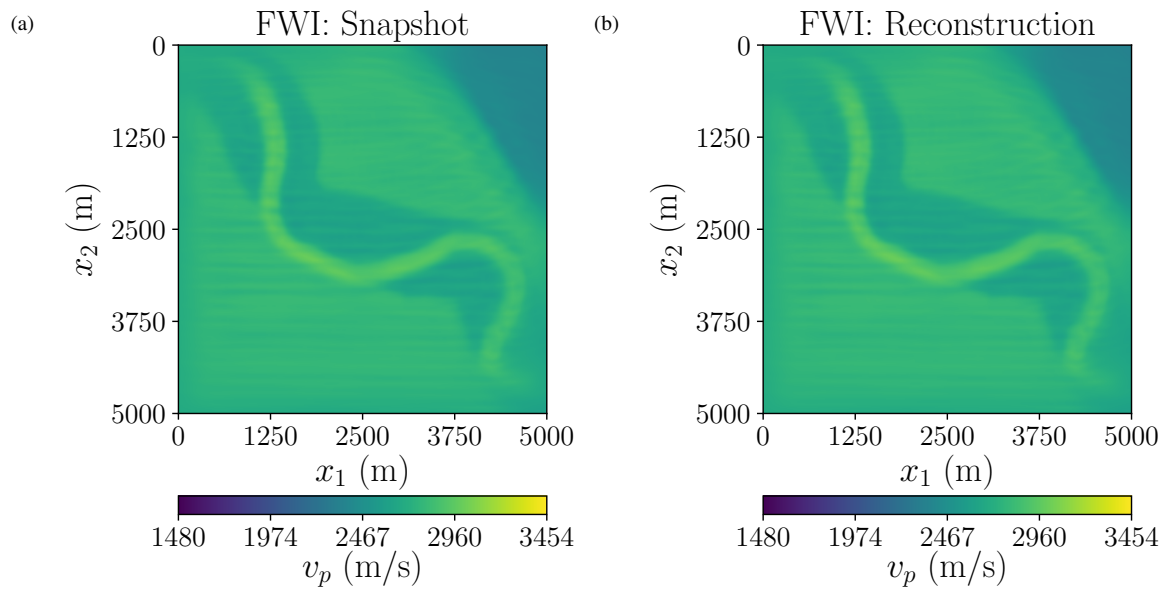

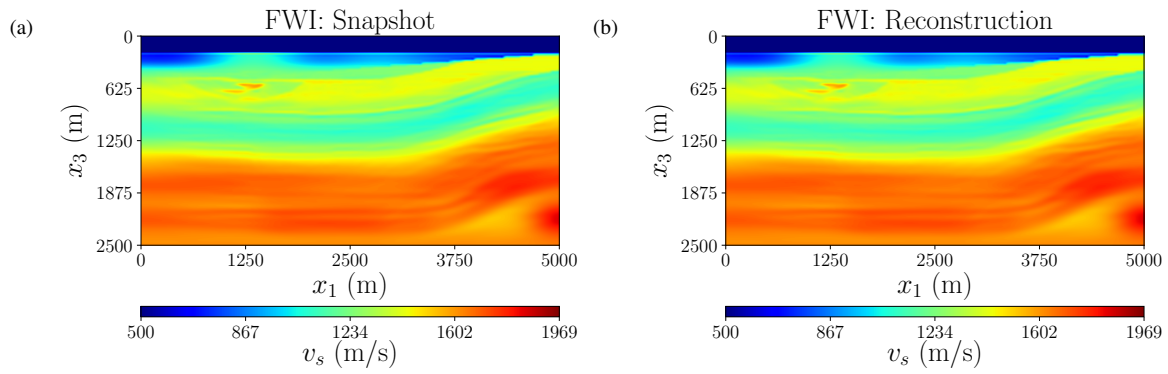Fig. 7: The inverted v_p distributions at $x_3 = 575$ m using a) wavefield snapshots and b) reconstruction.

Fig. 8: The inverted v_s distributions at $x_2 = 1250$ m using a) wavefield snapshots and b) reconstruction. The lower end of the colorscale has been clipped; the v_s velocity of the waterlayer is zero.
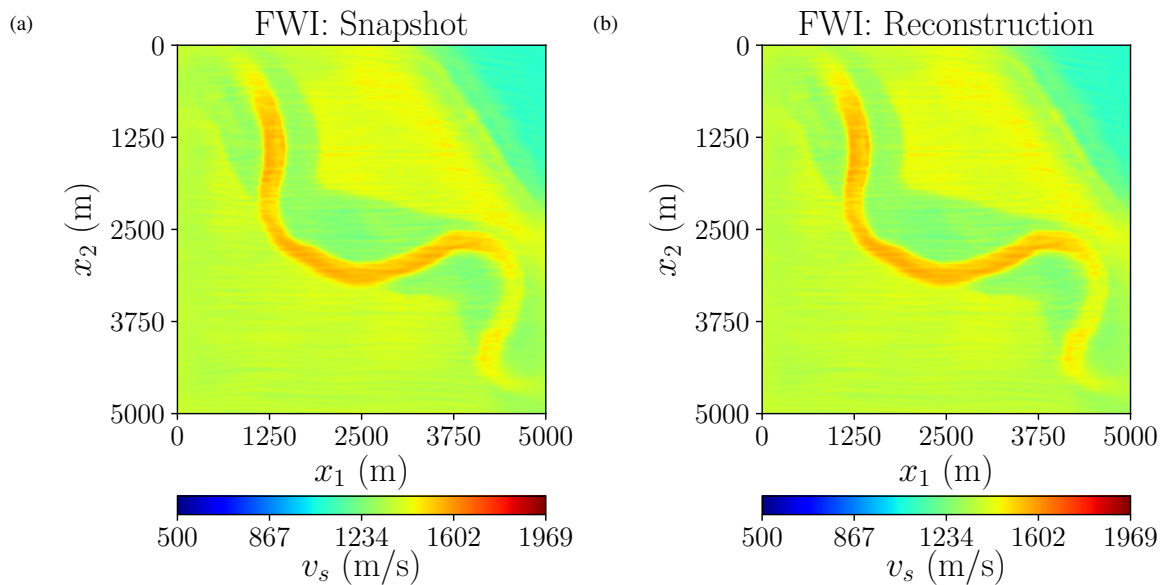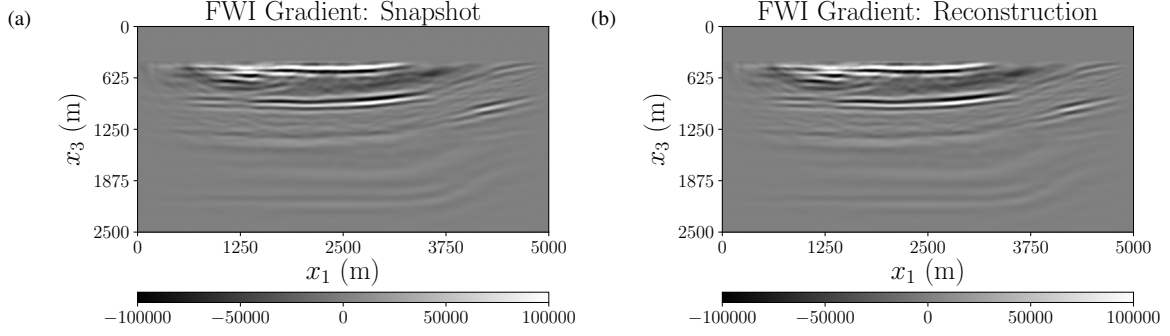

Fig. 9: The inverted v_s distributions at $x_2 = 575$ m using a) wavefield snapshots and b) reconstruction. The lower end of the colorscale has been clipped; the v_s velocity of the waterlayer is zero.

Fig. 10: The v_s gradient at the first iteration of the first shot batch using a) wavefield snapshots and b) reconstruction. Slice at $x_2 = 1250$ m.
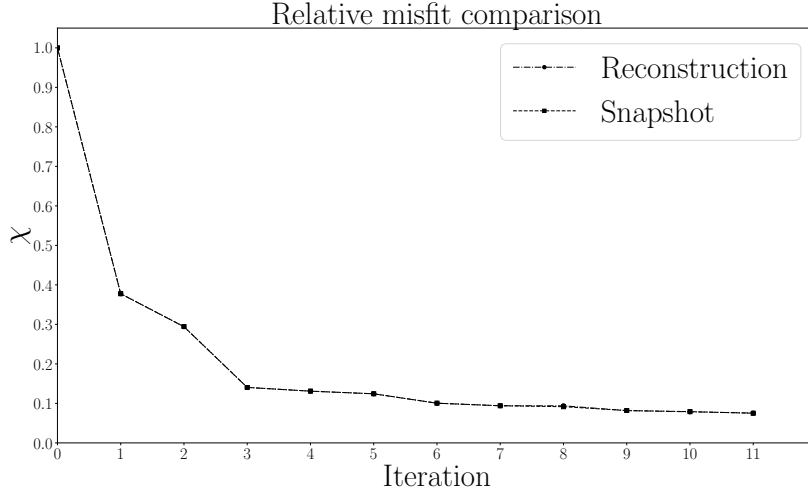

Fig. 11: The misfit evolutions of the inversion runs using wavefield reconstruction and wavefield snapshots for the first shot batch, for the 12 iterations in common.

APPENDIX A: RELATION TO THE MULTIPLE POINT SOURCES APPROACH

In order to demonstrate that the modified source functions in equations 23 and 24 are equivalent to the Multiple Point Sources approach of Vasmel & Robertsson (2016), we re-start our derivations at equation 11. After renaming indices and coordinates as done later in the main text, the latter equation reads

$$\hat{G}_{pq,nm}^{\tau,h}(\mathbf{x};\mathbf{x}_s) = \oint_{\partial\Omega} d^2\mathbf{x}_r \left(\{\hat{G}_{ij,pq}^{\tau,h}(\mathbf{x}_r;\mathbf{x})\}^* \hat{G}_{i,nm}^{v,h}(\mathbf{x}_r;\mathbf{x}_s) + \hat{G}_{ij,nm}^{\tau,h}(\mathbf{x}_r;\mathbf{x}_s)\{\hat{G}_{i,pq}^{v,h}(\mathbf{x_r};\mathbf{x})\}^* \right) n_j.$$

(A.1)

Rather than rewriting both instances of the anti-causal Green's function in terms of stress due to a source of deformation rate, we utilize the reciprocal relation

$$\hat{G}_{n,pq}^{v,h}(\mathbf{x}_B;\mathbf{x}_A) = \hat{G}_{pq,n}^{\tau,f}(\mathbf{x}_A;\mathbf{x}_B), \tag{A.2}$$

such that we achieve

$$\hat{G}_{pq,nm}^{\tau,h}(\mathbf{x};\mathbf{x}_s) = \int_\Omega d^3\mathbf{x}' \left\{\hat{G}_{pq,ij}^{\tau,h}(\mathbf{x};\mathbf{x}')\right\}^* \oint_{\partial\Omega} d^2\mathbf{x}_r \, \delta(\mathbf{x}'-\mathbf{x}_r)\hat{G}_{i,nm}^{v,h}(\mathbf{x}_r;\mathbf{x}_s)n_j$$
$$+ \int_\Omega d^3\mathbf{x}' \left\{\hat{G}_{pq,i}^{\tau,f}(\mathbf{x};\mathbf{x}')\right\}^* \oint_{\partial\Omega} d^2\mathbf{x}_r \, \delta(\mathbf{x}'-\mathbf{x}_r)\hat{G}_{ij,nm}^{\tau,h}(\mathbf{x}_r;\mathbf{x}_s)n_j. \tag{A.3}$$

The anti-causal Huygen's principle in equation 17 does not explicitly state how to handle reconstruction using two different types of Green's functions and source functions. However, from the reciprocity theorem of correlation type we can derive an anti-causal Huygen's principle for the stress field $\hat{\tau}_{pq}$ due to a source of deformation rate *and* a source of body force

$$\hat{\tau}_{pq}(\mathbf{x}) = \int_\Omega d^3\mathbf{x}' \left\{\hat{G}_{pq,ij}^{\tau,h}(\mathbf{x};\mathbf{x}')\right\}^* \{-\hat{h}_{ij}(\mathbf{x}')\} + \int_\Omega d^3\mathbf{x}' \left\{\hat{G}_{pq,i}^{\tau,f}(\mathbf{x};\mathbf{x}')\right\}^* \hat{f}_i(\mathbf{x}'). \tag{A.4}$$

Note that the reciprocial relation $\hat{G}_{n,pq}^{v,h}(\mathbf{x}_B;\mathbf{x}_A) = \hat{G}_{pq,n}^{\tau,f}(\mathbf{x}_A;\mathbf{x}_B)$ of equation A.2 has been used. Hence, we can reconstruct the Green's function $\hat{G}_{pq,nm}^{\tau,h}(\mathbf{x};\mathbf{x}_s)$ and the associated particle velocity by injecting the following source functions

$$\hat{\mathcal{F}}_{i,nm}^{MPS}(\mathbf{x};\mathbf{x}_s) = \oint_{\partial\Omega} d^2\mathbf{x}_r \left(\delta(\mathbf{x}-\mathbf{x}_r)\hat{G}_{ie,nm}^{\tau,h}(\mathbf{x}_r;\mathbf{x}_s)n_e\right), \tag{A.5}$$

$$\hat{\mathcal{H}}_{kl,nm}^{MPS}(\mathbf{x};\mathbf{x}_s) = \oint_{\partial\Omega} d^2\mathbf{x}_r \left(-\delta(\mathbf{x}-\mathbf{x}_r)\hat{G}_{k,nm}^{v,h}(\mathbf{x}_r;\mathbf{x}_s)n_l\right), \tag{A.6}$$

as sources of body force and deformation rate, respectively. These are the elastodynamic generalizations of the source functions in Vasmel & Robertsson (2016). Comparing the MPS sources (equations A.5-A.6) to the source functions in equations 23 and 24, we observe that the sources of deformation rate are exactly equal. The body force source sources differ by a factor $\rho(\mathbf{x})$ outside and a factor $\frac{1}{\rho(\mathbf{x}_r)}$ inside the integral. Considering the sifting properties and the infinitely compact support of the Dirac delta distribution, it is straightforward to show that also the body force sources are *analytically* exactly equal.

APPENDIX B: RECONSTRUCTION USING THE GREEN'S FUNCTION IN TERMS OF PARTICLE VELOCITY DUE TO A SOURCE OF BODY FORCE

For the reciprocity theorem of correlation type we consider the following source functions

$$\hat{f}_{i,A}(\mathbf{x},\omega) = \delta_{iq}\delta(\mathbf{x}-\mathbf{x}_A), \tag{B.1}$$

$$\hat{f}_{i,B}(\mathbf{x},\omega) \;=\; \delta_{ip}\delta(\mathbf{x}-\mathbf{x}_B). \tag{B.2}$$

The sources of deformation rate density are chosen to be equal to zero for both states. Performing essentially the same procedure as in the main text, we achieve a representation

$$\hat{G}^{v,f}_{p,q}(\mathbf{x};\mathbf{x}_s) + \chi(\mathbf{x}_B)\{\hat{G}^{v,f}_{p,q}(\mathbf{x};\mathbf{x}_s)\}^* = - \int_{\Omega} d^3\mathbf{x}' \left\{\hat{G}^{v,f}_{p,i}(\mathbf{x};\mathbf{x}')\right\}^* \oint_{\partial\Omega} d^2\mathbf{x}_r \left(\delta(\mathbf{x}'-\mathbf{x}_r)\hat{G}^{\tau,f}_{ij,q}(\mathbf{x}_r;\mathbf{x}_s)n_j \right.$$
$$\left. + \partial_l'\delta(\mathbf{x}'-\mathbf{x}_r)c_{mjil}(\mathbf{x}_r)\frac{\hat{G}^{v,f}_{m,q}(\mathbf{x}_r;\mathbf{x}_s)}{j\omega}n_j\right). \tag{B.3}$$

The Green's function in terms of particle velocity due to a source of body force satisfies the following hyperbolic wave equation

$$\hat{\mathcal{L}}_{im}(\mathbf{x})\hat{G}^{v,f}_{m,q}(\mathbf{x};\mathbf{x}') = -j\omega\hat{f}_i(\mathbf{x}) = -j\omega\delta_{iq}\delta(\mathbf{x}-\mathbf{x}'), \tag{B.4}$$

with the linear wave equation operator being given by

$$\hat{\mathcal{L}}_{im}(\mathbf{x})[\cdot] = \omega^2\rho\,\delta_{im}[\cdot] + \partial_j c_{ijkl}(\partial_k\delta_{ml}[\cdot]). \tag{B.5}$$

The corresponding anti-causal Huygen's principle for the particle velocity $\hat{v}_m$ reads

$$\hat{v}_m(\mathbf{x}) = \int_{\Omega} d^3\mathbf{x}' \left\{\hat{G}^{v,f}_{m,p}(\mathbf{x};\mathbf{x}')\right\}^* \{-\hat{f}_p(\mathbf{x}')\}. \tag{B.6}$$

The body force term in equation B.3 is therefore recognized as

$$\hat{f}_{i,q}(\mathbf{x};\mathbf{x}_s) = \oint_{\partial\Omega} d^2\mathbf{x}_r \left(\partial_l\delta(\mathbf{x}-\mathbf{x}_r)c_{mjil}(\mathbf{x}_r)\frac{\hat{G}^{v,f}_{m,q}(\mathbf{x}_r;\mathbf{x}_s)}{j\omega}n_j + \delta(\mathbf{x}-\mathbf{x}_r)\hat{G}^{\tau,f}_{ij,q}(\mathbf{x}_r;\mathbf{x}_s)n_j\right). \tag{B.7}$$

Consistent with the results of the main text, we note here a term which is not available from the forward modelling. The source function therefore requires analytical modifications. The frequency domain velocity-stress system with the given source function for wavefield reconstruction reads

$$j\omega\rho(\mathbf{x})\hat{G}^{v,f}_{i,q}(\mathbf{x};\mathbf{x}_s) - \partial_j\hat{G}^{\tau,f}_{ij,q}(\mathbf{x};\mathbf{x}_s) = \oint_{\partial\Omega} d^2\mathbf{x}_r \left(\partial_l\delta(\mathbf{x}-\mathbf{x}_r)c_{mjil}(\mathbf{x}_r)\frac{\hat{G}^{v,f}_{m,q}(\mathbf{x}_r;\mathbf{x}_s)}{j\omega}n_j\right.$$
$$\left. + \delta(\mathbf{x}-\mathbf{x}_r)\hat{G}^{\tau,f}_{ij,q}(\mathbf{x}_r;\mathbf{x}_s)n_j\right), \tag{B.8}$$

and

$$j\omega\hat{G}^{\tau,f}_{ij,q}(\mathbf{x};\mathbf{x}_s) - c_{ijkl}(\mathbf{x})\partial_l\hat{G}^{v,f}_{k,q}(\mathbf{x};\mathbf{x}_s) = 0. \tag{B.9}$$

Consider then the (possibly) modified fields $\hat{\mathcal{V}}_{i,q}(\mathbf{x};\mathbf{x}_s)$ and $\hat{\mathcal{T}}_{ij,q}(\mathbf{x};\mathbf{x}_s)$, defined in the same inhomogenous anisotropic medium as $\hat{G}^{v,f}_{i,q}(\mathbf{x};\mathbf{x}_s)$ and $\hat{G}^{\tau,f}_{ij,q}(\mathbf{x};\mathbf{x}_s)$, satisfying

$$j\omega\rho\hat{\mathcal{V}}_{i,q} - \partial_j\hat{\mathcal{T}}_{ij,q} = \hat{\mathfrak{f}}_{i,q}, \tag{B.10}$$

$$j\omega\hat{\mathcal{T}}_{ij,q} - c_{ijkl}\partial_l\hat{\mathcal{V}}_{k,q} = \hat{\mathfrak{s}}_{ij,q}. \tag{B.11}$$

The source function of body force and stress rate are respectively

$$\hat{\mathfrak{f}}_{i,q}(\mathbf{x};\mathbf{x}_s) = \oint_{\partial\Omega} d^2\mathbf{x}_r \left(\delta(\mathbf{x}-\mathbf{x}_r)\hat{G}^{\tau,f}_{ij,q}(\mathbf{x}_r;\mathbf{x}_s)n_j \right), \tag{B.12}$$

and

$$\hat{\mathfrak{s}}_{ij,q}(\mathbf{x};\mathbf{x}_s) = \oint_{\partial\Omega} d^2\mathbf{x}_r \left(\delta(\mathbf{x}-\mathbf{x}_r)c_{iekj}(\mathbf{x}_r)\hat{G}^{v,f}_{k,q}(\mathbf{x}_r;\mathbf{x}_s)n_e \right). \tag{B.13}$$

Isolating $\hat{\mathcal{T}}_{ij,q}$ in equation B.11 and inserting this quantity into equation B.10 gives

$$j\omega\rho\hat{\mathcal{V}}_{i,q}(\mathbf{x};\mathbf{x}_s) - \frac{1}{j\omega}\partial_j c_{ijkl}\partial_l\hat{\mathcal{V}}_{k,q}(\mathbf{x};\mathbf{x}_s) = \oint_{\partial\Omega} d^2\mathbf{x}_r \left(\partial_j\delta(\mathbf{x}-\mathbf{x}_r)c_{iekj}(\mathbf{x}_r)\frac{\hat{G}^{v,f}_{k,q}(\mathbf{x}_r;\mathbf{x}_s)}{j\omega}n_e \right.$$
$$\left. + \delta(\mathbf{x}-\mathbf{x}_r)\tau_{ij}(\mathbf{x}_r)n_j \right). \tag{B.14}$$

The term $\frac{1}{j\omega}\partial_j c_{ijkl}(\mathbf{x})\partial_l\hat{\mathcal{V}}_{k,q}(\mathbf{x};\mathbf{x}_s)$ is recognized as $\partial_j\hat{G}^{\tau,f}_{ij,q}(\mathbf{x};\mathbf{x}_s)$ if and only if $\hat{\mathcal{V}}_{i,q}(\mathbf{x};\mathbf{x}_s) = \hat{G}^{v,f}_{i,q}(\mathbf{x};\mathbf{x}_s)$. For now, assume that this is true. Renaming of the summation indices inside the first source term in equation B.14 and usage of the symmetry properties of the stiffness tensor suffice to show that equations B.14 and B.8 are indeed equal. The assumed equivalence therefore holds. Simultaneous usage of the source functions of body force and stress rate in equations B.10 and B.11 therefore yield the same wavefield reconstruction as the source function of body force in equation B.8. When inserted into the velocity-stress system, the source functions in equations B.10 and B.11 give source contributions that are analytically exactly equal to those derived in the main text.

APPENDIX C: ON THE UNIMPORTANCE OF THE PHYSICAL SOURCE TYPE

The main text discusses reconstruction of the Green's functions in terms of stress and particle velocity due to a source of deformation rate. Here, we briefly demonstrate that a physical source of body force leads to no modification of the reconstruction-type source function.

The following source functions are considered

$$\hat{h}_{ij,A}(\mathbf{x},\omega) = \delta(\mathbf{x}-\mathbf{x}_A)\frac{1}{2}\{\delta_{ip}\delta_{jq} + \delta_{iq}\delta_{jp}\}, \tag{C.1}$$

$$\hat{f}_{i,B}(\mathbf{x},\omega) = \delta(\mathbf{x}-\mathbf{x}_B)\delta_{in}, \tag{C.2}$$

which upon insertion into the correlation type reciprocity theorem (equation 8) gives, in similarity with equation 11,

$$\hat{G}^{\tau,f}_{pq,n}(\mathbf{x}_A;\mathbf{x}_B) - \chi(\mathbf{x}_B)\{\hat{G}^{v,h}_{n,pq}(\mathbf{x}_B;\mathbf{x}_A)\}^* =$$
$$\oint_{\partial\Omega} d^2\mathbf{x} \left(\{\hat{G}^{\tau,h}_{ij,pq}(\mathbf{x};\mathbf{x}_A)\}^*\hat{G}^{v,f}_{i,n}(\mathbf{x};\mathbf{x}_B) + \hat{G}^{\tau,f}_{ij,n}(\mathbf{x};\mathbf{x}_B)\{\hat{G}^{v,h}_{i,pq}(\mathbf{x};\mathbf{x}_A)\}^* \right)n_j. \tag{C.3}$$

With $\mathbf{x}_B \in \Omega$, the left-hand side retrieves, as before, a homogenous Green's function

$$\hat{\mathcal{G}}_{pq,n}^{\tau,f}(\mathbf{x}_A;\mathbf{x}_B) := \hat{G}_{pq,n}^{\tau,f}(\mathbf{x}_A;\mathbf{x}_B) - \{\hat{G}_{pq,n}^{\tau,f}(\mathbf{x}_A;\mathbf{x}_B)\}^*, \tag{C.4}$$

The reciprocal relation in equation A.2 has been used. The homogenous Green's function in terms of stress due to a body force source satisfies the wave equation

$$\begin{aligned}
\hat{\mathcal{L}}_{klpq}(\mathbf{x})\hat{\mathcal{G}}_{pq,n}^{\tau,f}(\mathbf{x};\mathbf{x}_s) &= \delta(\mathbf{x}-\mathbf{x}_s)\Big\{\frac{1}{2}\partial_l\big(\frac{1}{\rho(\mathbf{x})}\delta_{kn}\big) - \frac{1}{2}\partial_k\big(\frac{1}{\rho(\mathbf{x})}\delta_{ln}\big)\Big\} \\
&\quad - \delta^*(\mathbf{x}-\mathbf{x}_s)\Big\{\frac{1}{2}\partial_l\big(\frac{1}{\rho(\mathbf{x})}\delta_{kn}\big) - \frac{1}{2}\partial_k\big(\frac{1}{\rho(\mathbf{x})}\delta_{ln}\big)\Big\}^* \\
&= 0, \tag{C.5}
\end{aligned}$$

with $\hat{\mathcal{L}}_{klpq}(\mathbf{x})$ given by equation 16. Equation C.3 is therefore exactly analogous to equation 11, but replacing the source type in the state to be reconstructed. From the anti-causal Huygen's principle (equation 17) we observe that the inverse extrapolation is independent of the physical source. No modifications to the reconstruction-type source functions are therefore needed to handle different types of *physical* sources.